Materials Characterization 142 (2018) 432–442

Contents lists available at ScienceDirect

Materials Characterization

journal homepage: www.elsevier.com/locate/matchar

Formation of intermetallic structures at the interface of steel-to-aluminium explosive welds☆

G.H.S.F.L. Carvalho[a], I. Galvão[a,b,*], R. Mendes[c], R.M. Leal[a,d], A. Loureiro[a]

[a] CEMMPRE, Department of Mechanical Engineering, University of Coimbra, Rua Luís Reis Santos, 3030-788 Coimbra, Portugal
[b] ISEL, Department of Mechanical Engineering, Polytechnic Institute of Lisbon, Rua Conselheiro Emídio Navarro, 1959-007 Lisboa, Portugal
[c] ADAI, LEDAP, Department of Mechanical Engineering, University of Coimbra, Rua Luís Reis Santos, 3030-788 Coimbra, Portugal
[d] ESAD.CR, Polytechnic Institute of Leiria, Rua Isidoro Inácio Alves de Carvalho, 2500-321 Caldas da Rainha, Portugal

ARTICLE INFO

Keywords:
Intermetallic phases
Interfacial characterisation
Explosive welding
Weldability
Steel-to-aluminium welding

ABSTRACT

The formation of intermetallic structures at the interface of carbon steel to 6082 aluminium alloy explosive welds and their influence on the weldability of these two materials were studied. The morphology, the microstructure, the chemical and phase compositions of the welds were characterised by several types of microscopy techniques. The interface characterisation proved that explosive mixtures with a lower detonation velocity were revealed as being more suitable for achieving consistent welds since jet entrapment was prevented and continuous molten layers were not formed at the weld interface. It was also found that the physical properties of the intermetallic phases generated at the weld interface have a strong influence on the weldability of steel-to-aluminium explosive welds. Specifically, it was shown that the formation of aluminium-rich intermetallic phases at the weld interface increases the solidification time of the interfacial molten material, decreasing the weldability of these two materials. The formation of these intermetallic compounds should be avoided by reducing the interaction between the flyer and the baseplate as well as by avoiding excessive molten layers.

1. Introduction

Aluminium to steel (Al-Fe) joining has a very high economic and technical interest for many industries, since it makes possible to develop engineering solutions, which combine the lightweight and the high thermal and electrical conductivities of aluminium with the low cost and the high structural strength of steel. However, these metals are very difficult to join through the conventional welding techniques, because they present huge differences in their physical properties as well as having a very high susceptibility to generating brittle intermetallic phases. Sound joining of these materials requires that both the volume of the interacting material and the interaction time under high temperature are minimised. This may be achieved through explosive welding [1] and magnetic pulse welding [2], i.e. two impact-loading welding technologies, which, despite being conceptually different, share several operating principles. However, despite occurring in a very narrow region of the weld interface and for a very short time, the interaction of both materials also exists in these processes. So, it is crucial to characterise the morphological and the microstructural properties of the weld interface to understand the thermomechanical phenomena occurring at this zone, which have a decisive influence on the welding results [3].

The morphology of the Al-Fe weld interface has been characterised by many authors. Tricarico et al. [4], in explosive welding of AA5083 to ASTM A516 carbon steel plates, reported the formation of a wavy interface all along the weld length. However, most of the authors have reported the formation of a weld interface with a hybrid morphology, i.e. partially flat and partially wavy. Yu et al. [5], in magnetic pulse welding of AA3003 to AISI 1020 carbon steel tubes, reported the formation of an interface in which wavy regions were intercalated with flat regions along the weld length. In turn, Yu and Tong [6], in magnetic pulse welding of AA1060 to GB Q235 carbon steel base plates, instead of observing intercalated morphologies, detected both interface morphologies occurring simultaneously all along the weld length. A flat morphology was observed at the interface between the aluminium alloy and an Al-Fe mixed layer, which was formed between both welded metals, and a wavy morphology was observed at the interface between this layer and the steel plate.

☆ We wish to confirm that there are no known conflicts of interest associated with this publication. We confirm that the manuscript has been read and approved by all named authors and we further confirm that the order of authors listed in the manuscript has been approved by all of us.

* Corresponding author at: CEMMPRE, Department of Mechanical Engineering, University of Coimbra, Rua Luís Reis Santos, 3030-788 Coimbra, Portugal.
E-mail addresses: gustavo.carvalho@student.dem.uc.pt (G.H.S.F.L. Carvalho), ivan.galvao@dem.uc.pt (I. Galvão), ricardo.mendes@dem.uc.pt (R. Mendes), rui.leal@dem.uc.pt (R.M. Leal), altino.loureiro@dem.uc.pt (A. Loureiro).

https://doi.org/10.1016/j.matchar.2018.06.005
Received 21 April 2018; Received in revised form 28 May 2018; Accepted 3 June 2018
Available online 04 June 2018
1044-5803/

Some studies have already been performed to characterise the microstructure of the weld interface, and especially, the properties of the aforementioned Al-Fe layer, which is also denominated the transition or intermediate region. Li et al. [7], in explosive welding of AA5083 to GB Q345 low-alloy steel plates, reported the formation of discontinuous transition regions, which were intercalated with direct bonding zones. The transition regions were reported to present a molten morphology and to be composed of the intermetallic phases $FeAl_2$ and Fe_2Al_5. In turn, Aizawa et al. [8] reported the formation of two different transition regions in explosive welding of AA1100 to JIS SPCC carbon steel plates, which were formed at the rear and the front sides of the interfacial waves. In agreement with Li et al. [7], the rear side regions, in which dendrite branches, voids, and cracks were observed, were reported to result from localised melting and solidification. The intermetallic phases Fe_2Al_5 and $FeAl_3$ were identified in these regions. On the other hand, no evidence of local melting was observed on the front side transition zones, which were composed of a dispersion of Fe particles over an Al matrix. The authors reported that these regions were formed by Al-Fe mixing in a solid state.

A few recent studies have also addressed the crystallinity of the Al-Fe transition layer to further understand the metallurgical phenomena occurring at the weld interface. Fan et al. [9], in magnetic-pulse welding of AA1060 to AISI 1020 carbon steel tubes, reported the formation of an amorphous layer, with a few nanometres, at the Al/Fe interface. Although no intermetallic phases were detected, the interdiffusion of the Al and Fe elements across the interface promoted a composition gradient in this layer. According to the authors, the loss of crystalline structure within the interfacial layer was induced by the instability of the mechanical lattice during the high-strain-rate impact and by interdiffusion at temperatures below the melting temperature. The amorphisation of the transition layer was also reported by Yu et al. [10], in magnetic pulse welding of 5A02 aluminium alloy to AISI 304 stainless steel tubes. The transition layer was reported to be composed of an amorphous Al-rich matrix in which a nanoscale Fe-rich ordered phase was scattered.

Although some work on the weld interface characterisation has already been conducted, the influence of the formation of interfacial intermetallic structures on the Al-Fe weldability by impact welding remains unexplored. So, the aim of the present research is to study the formation of intermetallic structures at the interface of carbon steel to AA6082 explosive welds and their influence on the weldability of these materials. The morphology, the microstructure, the chemical and phase compositions of the welds were characterised using several characterisation techniques, such as optical microscopy, scanning electron microscopy (SEM), energy dispersive spectroscopy (EDS), electron backscatter diffraction (EBSD), and microhardness testing.

2. Experimental Procedure

Four series of Al-Fe explosive welds were produced by projecting 3 mm-thick plates of EN DC06 carbon steel over 15 mm-thick plates of AA6082-T6. The hardness values of the carbon steel and the aluminium alloy are 116 $HV_{0.2}$ and 111 $HV_{0.2}$, respectively. All the welds were produced in a full overlap joint configuration. Regarding the explosive mixture, two weld series were produced with an ANFO-based mixture and two series were produced with explosive emulsion-based mixtures (EE). The explosive emulsion mixtures were sensitized with hollow glass microspheres (HGMS) in one series and with expanded polystyrene (EPS) in the other series. The use of these sensitizers in explosive welding was studied in detail by Mendes et al. [11]. Different explosive to flyer mass ratios (explosive ratios) were used in the four weld series. The stand-off distance was the same in all welds. The welding conditions are summarised in Table 1. As displayed in the table, the nomenclature used for labelling the welds identifies the explosive mixture and ratio. For example, the EE-PS5 weld was produced with the explosive emulsion sensitized with EPS, using an explosive ratio of 0.53, and the AF-9 weld was produced with ANFO, using an explosive ratio of 0.93.

Table 1
Welding parameters of the EE and AF welds.

	Welds			
	EE-PS5	*EE-HG6*	*AF-9*	*AF-6*
Flyer plate alloy	EN DC06 steel	EN DC06 steel	EN DC06 steel	EN DC06 steel
Base plate alloy	AA6082-T6	AA6082-T6	AA6082-T6	AA6082-T6
Configuration	Full overlap	Full overlap	Full overlap	Full overlap
Explosive	EE + EPS	EE + HGMS	ANFO	ANFO
Flyer plate thickness	3 mm	3 mm	3 mm	3 mm
Base plate thickness	15 mm	15 mm	15 mm	15 mm
Explosive ratio	0.53	0.68	0.93	0.69
Stand-off distance	4.5 mm	4.5 mm	4.5 mm	4.5 mm

The detonation velocity of the explosive mixtures was measured following the procedure reported in Mendes et al. [12] for all the weld series. After welding, samples were removed longitudinally to the welding direction and prepared for metallographic analysis according to ASTM E3-11. A Leica DM4000M LED optical microscope was used to observe the welds. The microstructural characterisation was complemented by SEM, using a field emission scanning electron microscope, Zeiss Merlin VP Compact. This equipment was provided with EDS, which was used to analyse the chemical composition of the weld interface. The phase composition of the weld interface was analysed by EBSD, using a field emission scanning electron microscope, FEI Quanta 400FEG ESEM/EDAX Genesis X4M. The indexing of the EBSD patterns was conducted using Genesis and Delphi software applications. The mechanical properties of the welds were characterised by microhardness testing, which was conducted using Struers Duramin equipment. Measurements with a testing load of 25 g were performed at the weld interface.

3. Results and Discussion

3.1. Welding Parameters and Weldability Window

Table 2 shows the values measured for the detonation velocity (V_d) and the values calculated for the impact velocity (V_p) and the collision angle (β). V_p and β were computed using the Gurney equation for a dimensional problem in parallel configuration (Eq. (01)) [13, 14] and with a relation between both velocities and β (Eq. (02)) [13].

$$V_p = \sqrt{2E}\cdot\sqrt{\frac{3R^2}{R^2 + 5R + 4}} \quad (01)$$

$$\beta = 2\cdot\arcsin\left(\frac{V_p}{2\cdot V_d}\right) \quad (02)$$

R is the explosive ratio (dimensionless) and $\sqrt{2E}$ is the Gurney characteristic velocity of the explosive ($m\cdot s^{-1}$). This parameter was estimated through an empirical correlation obtained by Cooper [15] for ideal explosives, $\sqrt{2E} = V_d/2.97$.

Table 2
Values of detonation velocity, impact velocity and collision angle for the EE and AF welds.

Welds	V_d (V_c) ($m\cdot s^{-1}$)	V_p ($m\cdot s^{-1}$)	β (°)
EE-PS5	3172	372	7
EE-HG6	3514	497	8
AF-9	2300	404	10
AF-6	2072	296	8

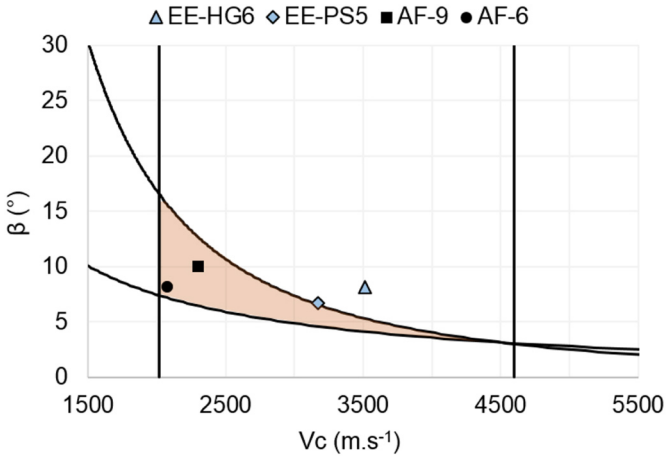

Fig. 1. Weldability window obtained for the EE and AF welds.

Based on previous research [12], the detonation velocity of the explosive mixtures was found to be strongly influenced by the explosive type. Much higher detonation velocity values were registered in the welds produced with the explosive emulsion. In turn, the calculated impact velocity and collision angle were found to be influenced by both the type of explosive and the explosive ratio (Eqs. (01) and (02)).

Fig. 1 shows the weldability window obtained for the carbon steel-AA6082 pair. This tool is a graphical approach that relates the collision point velocity to the β angle. It is composed of four limits: The left, lower and upper limits were computed according to Eq. (03) [16], Eq. (04) [17] and Eq. (05) [18], respectively. The right limit was plotted by defining the maximum V_c for jetting formation as the bulk sound speed in the material [19].

$$R_T = \frac{(\rho_{flyer} + \rho_{base})\cdot V_c^2}{2\cdot(H_{flyer} + H_{base})} \quad (03)$$

R_T is the Reynolds number, ρ_{flyer} and H_{flyer} are the density ($kg\cdot m^{-3}$) and the hardness (Pa) of the flyer plate, ρ_{base} and H_{base} are the same parameters of the baseplate.

$$\beta = k\cdot\sqrt{\frac{H_H}{\rho_{fb}\cdot V_c^2}} \quad (04)$$

k is a constant related to the surface roughness and cleanliness, H_H is the hardness of the harder material (Pa) and ρ_{fb} is the average density of the welded materials ($kg\cdot m^{-3}$).

$$V_p = \frac{1}{N}\frac{(T_{m\,flyer}\cdot C_{B\,flyer})^{1/2}}{V_c}\cdot\left(\frac{\lambda_{flyer}\cdot c_{flyer}\cdot C_{B\,flyer}}{\rho_{flyer}\cdot\delta_{flyer}}\right)^{1/4} \quad (05)$$

$T_{m\ flyer}$ is the melting temperature (°C), $C_{B\ flyer}$ is the bulk sound speed ($m\cdot s^{-1}$), λ_{flyer} is the thermal conductivity ($W\cdot m^{-1}\cdot K^{-1}$), c_{flyer} is the specific heat ($J\cdot kg^{-1}\cdot K^{-1}$), δ_{flyer} is the thickness (m) and N is a constant [20]. All these parameters concern the flyer plate.

Although the weldability window is a very empirical tool, especially developed for similar welding, it provides an indication of the requirements that enable the production of consistent welds, which corresponds to the graphical area inside the four limits. From Fig. 1 it can be observed that the AF welds are framed within the acceptable welding region. These welds are expected to be consistent, displaying continuous and wavy interfaces. On the other hand, the EE welds, which are framed above the top limit of the window, are expected to present excessive interfacial melting. Specifically, this limit was defined based on the Wittman condition [18], which establishes that no consistent welds are achieved if a continuous molten layer is formed at the weld interface.

3.2. Morphology and Microstructure of the Interface

Micrographs of the interface of the EE and AF welds are illustrated in Fig. 2. As summarised in Table 3, the interface of the welds presented important differences according to the welding conditions. Fig. 2a and b show that the interface of the EE welds is divided into two parts, i.e. the flyer and the baseplate separated after the impact. In agreement with the results of the weldability window (Fig. 1), no effective joining of the welded materials was found to occur at the interface of these welds. Regarding the welds produced with ANFO, the interface was found to be consistent. However, while the interface of the AF-9 weld was uniform along all the weld length (Fig. 2c), the interface of the AF-6 weld was consistent only for part of the length (Fig. 2d and e). These results are in partial agreement with the weldability window, since consistent welds, with effective joining along the entire interface, were expected for both the AF welding conditions.

As illustrated in Fig. 2, the interface of all the welds presented a flat morphology. Neither well-defined symmetrical waves, usually observed in similar welding [21], nor well-defined asymmetrical waves, already reported in Al-Fe [22] and Al-Cu welding [21], were formed at the interface of the welds. As indicated in Table 3, some irregularities, of very small amplitude, were observed at the interface of the EE-PS5 (Fig. 2a), EE-HG6 (Fig. 2b) and AF-9 (Fig. 2c) welds. This feature has already been reported in Cu-Al welding (copper as the flyer plate) [23]. Only the interface of the AF-6 weld, which was produced with the lowest detonation and impact velocities, presented a fully flat morphology without irregularities (Fig. 2d and e). The interface morphology of all welds is not in good agreement with the weldability window, since the welds were located on the right side of the Cowan limit (left limit in Fig. 1), and consequently, wavy interfaces were expected to form. However, the morphology observed concur with the conclusions from Carvalho et al. [24]. According to these authors, there is no formation of interfacial waves in welds where the flyer plate has a much higher density and melting temperature than the baseplate.

Regarding the microstructure of the welds, a flat and elongated grain structure was observed at the interface, especially for the steel (Fig. 2). This structure is widely reported in the literature and results from the strong plastic deformation promoted by the impact [8]. However, from Fig. 3, in which a SEM/EBSD micrograph of the interface of the EE-HG6 weld (registered on the steel side) is shown, it can be observed that the deformed grain structure evolves to a refined grain structure in the regions nearest to the weld interface. These two adjacent subzones result from a gradient in temperature and plastic deformation near the weld interface. The most extreme temperatures and pressures experienced in the regions nearest to the interface promoted the dynamic recrystallization of the grain, which led to the formation of a refined microstructure. As explosive welding is a very short-cycle process, the grains experienced a very fast thermal cycle, which prevented their growth [25].

Fig. 2 also shows the formation of a transition region at the interface of the welds. The morphology and the thickness of this region varied according to the welding conditions (Table 3). As illustrated in Fig. 2a and b, continuous transition layers were formed in the EE-PS5 and EE-HG6 welds. The average thickness of these layers was 33 μm (EE-PS5) and 48 μm (EE-HG6). In turn, much thinner transition regions were formed in the AF welds (Table 3). Fig. 2c and d show that these regions were not continuous, consisting of localised material pockets. Specifically, these pockets were even smaller and scarcer in the AF-6 weld, existing only in part of the weld length (Fig. 2d), where effective joining occurred. No signs of transition material were visible in the discontinuous part of this weld (Fig. 2e).

3.3. Composition of the Interface

Fig. 4 shows SEM micrographs of the transition regions of the welds. The chemical composition of these regions, which was analysed in the

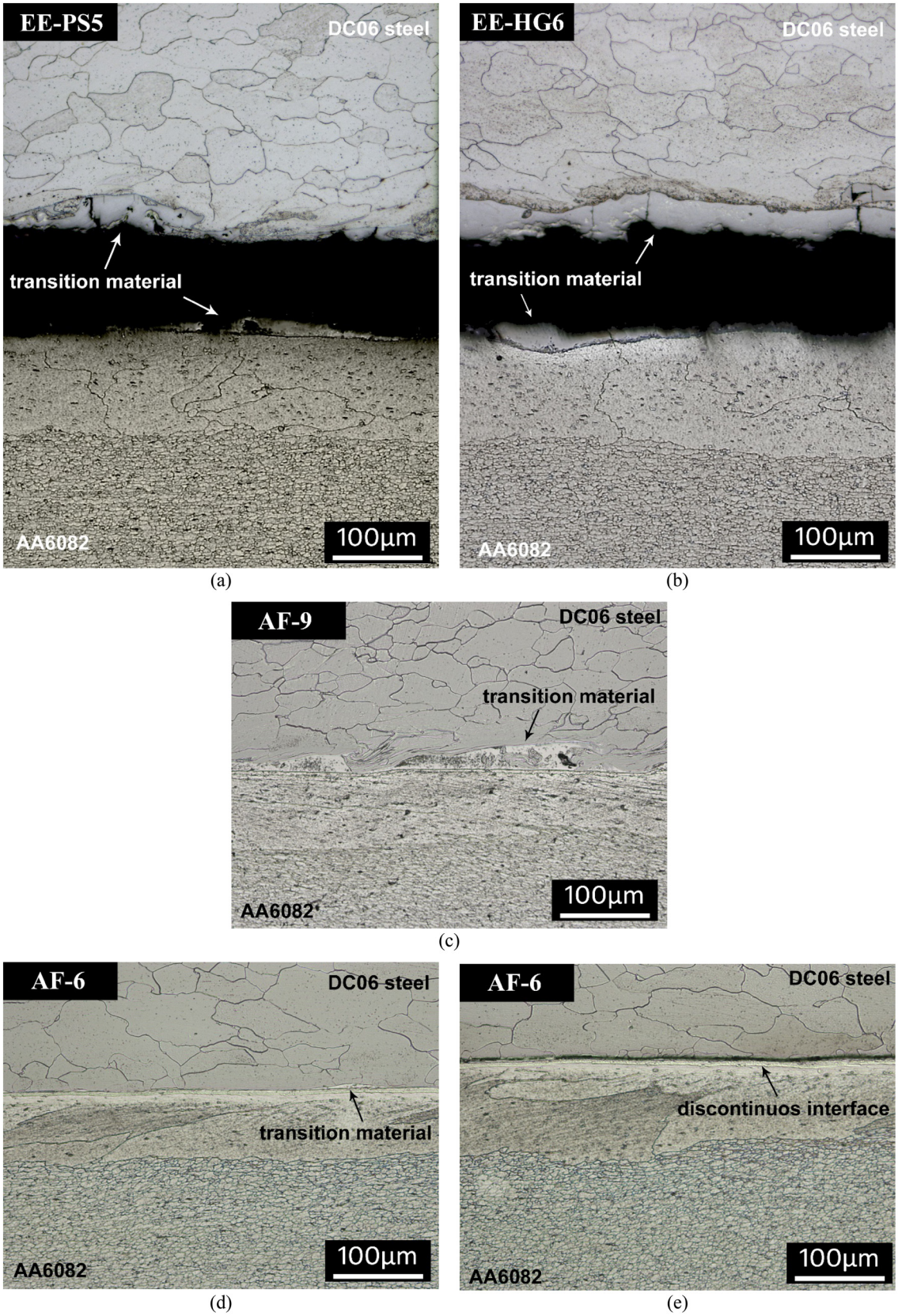

Fig. 2. Micrographs of the interface of the welds: (a) EE-PS5, (b) EE-HG6, (c) AF-9, (d, e) AF-6.

zones indicated in the micrographs (zones 1 to 9), is displayed in Table 4. It can be observed that the morphology of the transition layers of the EE-PS5 (Fig. 4a and b) and EE-HG6 (Fig. 4c and d) welds is very similar. Most of the area of these layers is composed of a light grey material, although some darker regions can also be observed. According to Table 4, the light grey material regions (zones 1 and 4 in Fig. 4b and

Table 3
Interface characteristics and thickness of the transition layer for the EE and AF welds.

Weld	Interface characteristics		
	Bonding	Morphology	Transition region (feature - avg. thickness)
EE-PS5	No	Flat with irregularities	Layer - 33 μm
EE-HG6	No	Flat with irregularities	Layer - 48 μm
AF-9	Uniform	Flat with irregularities	Localised pockets - 15 μm
AF-6	Non-uniform	Fully flat	Localised pockets - 2 μm

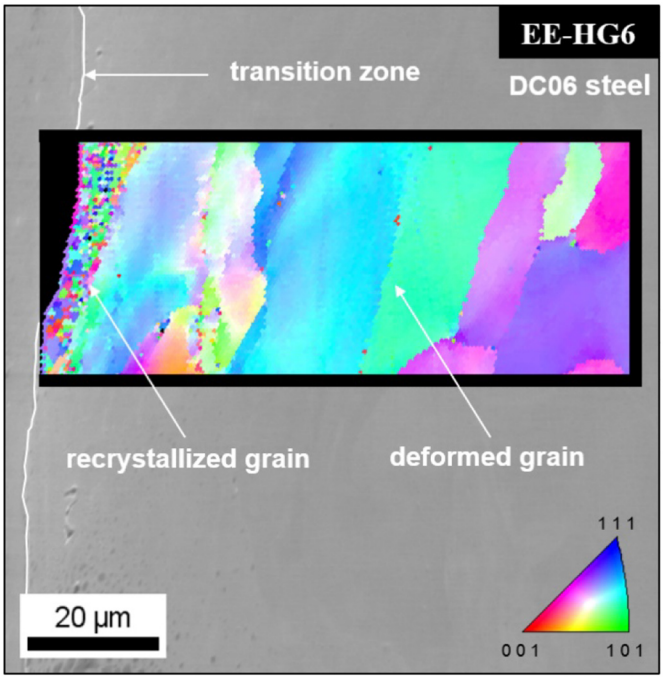

Fig. 3. SEM/EBSD micrograph registered at the interface of the EE-HG6 weld. (For interpretation of the references to color in this figure, the reader is referred to the web version of this article.)

d) present a hybrid Al-Fe chemical composition, which is richer in Al. In turn, the darker regions (zones 2 and 5 in Fig. 4b and d) are essentially composed of Al. Fig. 4a and c show that there are also some islands exclusively composed of Fe (Table 4, zone 3 in Fig. 4b) in the transition layer.

As illustrated in Fig. 5, the phase composition of the transition layer of the EE-HG6 weld was analysed by EBSD. The pictures on the left are the Kikuchi patterns acquired in the analysis zones indicated in Fig. 4c, whereas the pictures on the right are their indexed results. In the analysis zones I and II, which were performed in the aforementioned light grey hybrid regions, the intermetallic phase best matching the obtained patterns was Fe_4Al_{13}. In turn, the phase best matching the patterns acquired in the analysis zone III, which corresponds to the interface between the transition layer and the steel flyer, was Fe_2Al_5. As the software provided a consistent matching, it can be concluded that most of the transition layer of the EE-HG6 weld is composed of the Fe_4Al_{13} intermetallic phase. This suggests that, under extreme pressure, temperature and deformation, the diffusion of the elements was accelerated and a thick liquid film, rich in Fe_4Al_{13} was formed at the interface of the EE welds. The regions in the transition layers of the EE-PS5 and EE-HG6 welds with a different phase composition, such as the zones essentially composed of Al (black regions in Fig. 4b and d) and the regions rich in Fe_2Al_5, resulted from local heterogeneities in chemical composition. Specifically, the identification of the Fe_2Al_5 intermetallic phase near the steel flyer agrees well with the Fe-richer composition of this phase compared to the Fe_4Al_{13}.

Cracks propagating through the transition layers of the EE welds, which are blocked by the ductile steel islands located in these regions, can be observed in Fig. 4b and d. This is in good agreement with the brittle nature of the Al-rich intermetallic phases composing these zones [26]. As displayed in Table 5, the hardness values registered in these regions were found to range between about 260 $HV_{0.2}$ and 920 $HV_{0.2}$, which are well-above the hardness of both base metals. These hardness peaks coincide well with the values reported in the literature concerning Al-rich intermetallic phases [27, 28].

Fig. 4e shows the transition region of the AF-9 weld, corresponding to a localised material pocket (transition material in Fig. 3c). According to Table 4, this zone (zone 6 in Fig. 4e) is essentially composed of Al. Some small islands exclusively composed of Fe (zone 7 in Fig. 4e, Table 4) were also observed in this region. Both the thickness and the chemical composition of the transition region of the AF-9 weld, point to a reduced interaction of both welded materials at the interface. However, despite in much lesser extent than in the EE welds, formation of some intermetallic phases occurred at the weld interface. The dispersion of these compounds over the Al-rich volumes explains the high hardness values registered in these zones (Table 5). As illustrated in Fig. 4f, the transition region of the AF-6 weld was the less evident. A sharp chemical transition (zones 8 and 9, Table 4) was observed along most of the weld length, since localised material pockets were very scarce in this weld.

3.4. Analysis of the Interface Structure and Welding Parameters

In order to assess the thermomechanical conditions experienced at the weld interfaces, the values of the kinetic energy lost in the collision (ΔKE), which were computed according to Eq. (06), are displayed in Table 6.

$$\Delta KE = \frac{1}{2}\cdot m_{flyer}\cdot V_p^2 \quad (06)$$

m_{flyer} is the mass per unit area ($kg\cdot m^{-2}$) of the flyer plate.

As reported by Hokamoto et al. [29] and Hokamoto et al. [30], the energy lost at the weld interface has an important influence on the phenomena occurring in this zone. The differences observed in the ΔKE calculated values point to different conditions being experienced at the interfaces of the welds. The AF-6 weld, which was produced with the lowest collision point and impact velocities, presented a much lower interfacial energy than the other welds. This coincide with the structural and morphological properties of its interface, in which the most reduced interaction was registered, and no effective joining of the metals was achieved along all the weld length. As shown in Fig. 1, this weld was plotted inside the weldable region of the weldability window. However, it was located very close to the lower limit, which corresponds to the minimum impact pressure needed to produce the weld [17]. According to Plaksin et al. [31], the propagation of the detonation wave has an oscillatory nature, which is related to periodic variations in the values of the local detonation velocity. A local drop in the detonation/collision point velocity during welding may have been sufficient to shift the weld outside the weldable region. Because of this, the stresses arising locally near the point of contact may have been insufficient to overcome the strength properties of the materials. This promoted little or no bonding in some zones of the weld interface [17, 18].

According to the weldability window (Fig. 1), consistent joining was expected for the AF-9 weld and excessive interfacial melting was expected to the EE welds. In good agreement with this, thin and localised transition pockets were observed at the interface of the consistent AF-9 weld, whereas the interface of the non-consistent EE welds was composed of a thick and continuous molten layer. As displayed in Table 6, the interfacial energy value obtained for the EE-HG6 weld matches both

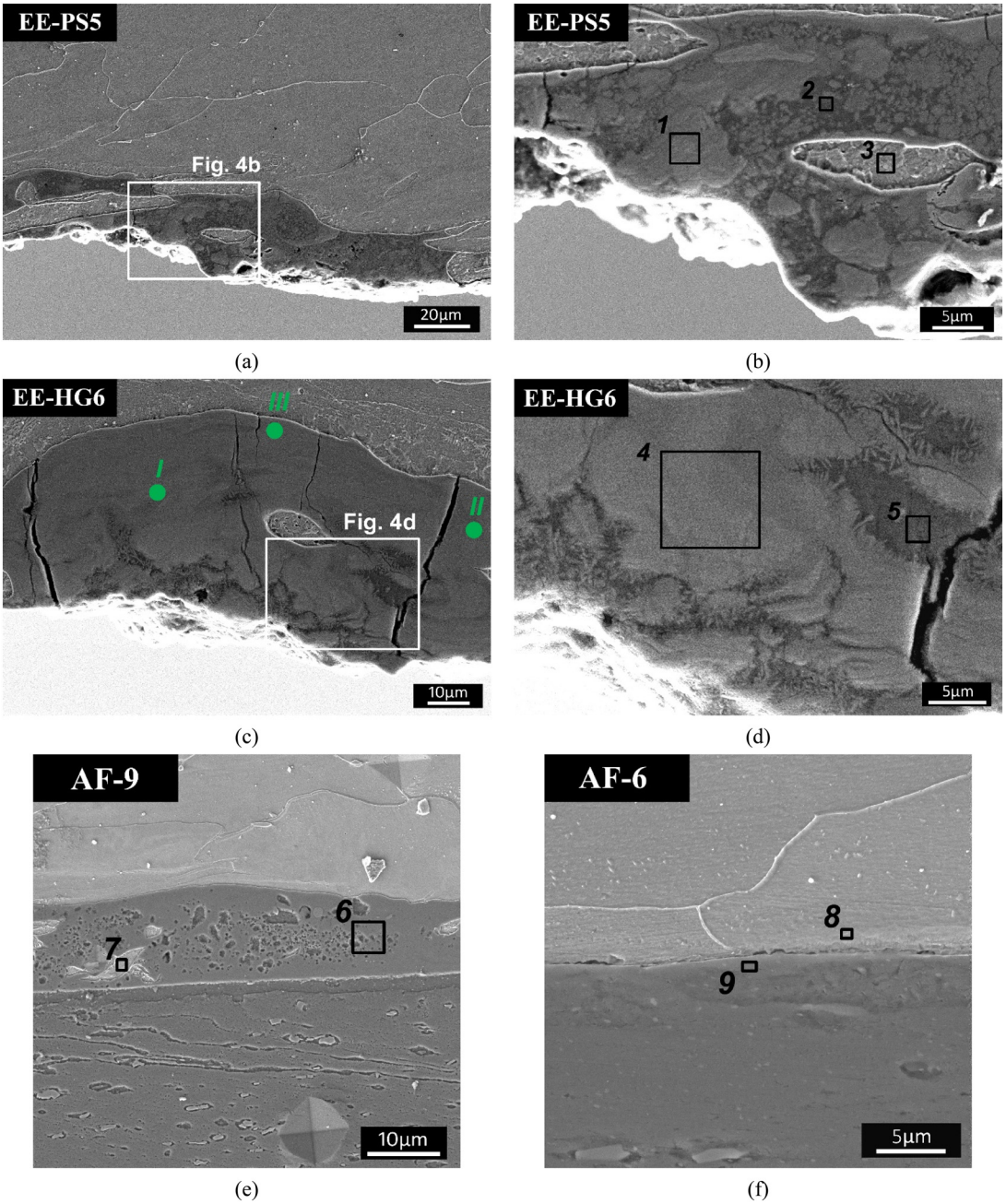

Fig. 4. SEM micrographs of the welds: (a, b) EE-PS5, (c, d) EE-HG6, (e) AF-9, (f) AF-6.

Table 4
Chemical composition registered in the interface of the EE and EF welds.

Weld	Analysis zone	Atomic %			
		Al	Fe	Si	Mg
EE-PS5	1	61.56	37.37	0.73	0.34
	2	92.75	5.46	0.93	0.86
	3	0.98	98.95	0.07	0.00
EE-HG6	4	57.70	41.29	0.78	0.23
	5	92.39	5.92	0.91	0.79
AF-9	6	92.44	5.95	0.99	0.62
	7	0.92	99.08	0.00	0.00
AF-6	8	–	100.0	–	–
	9	98.24	–	1.76	–

the weldability window and the microstructural results. However, comparing the interfacial energies and the microstructural properties of the EE-PS5 and AF-9 welds, it can be observed that excessive interfacial melting was observed only in the weld produced with a lower ΔKE value (and a lower impact velocity). This is explained by the differences in the collision point velocities of both welds. As the collision point velocity of the EE-PS5 weld was much higher than that of the AF-9 weld (Table 2), the volume of the interfacial jet entrapped within the weld structure was much higher in the EE-PS5 weld [32]. The continuous intermetallic layer observed at the interface of the EE welds results from this jet entrapment. It should be noted that the thickness of the jet is expected to be much lower than the thickness of the intermetallic layer. In fact, most of the energy dissipated at the interface goes initially into the kinetic energy of the jet and, subsequently to the entrapment of the jet, a large fraction of it is used to melt additional metal around the interface [33], promoting the formation of a thick molten layer.

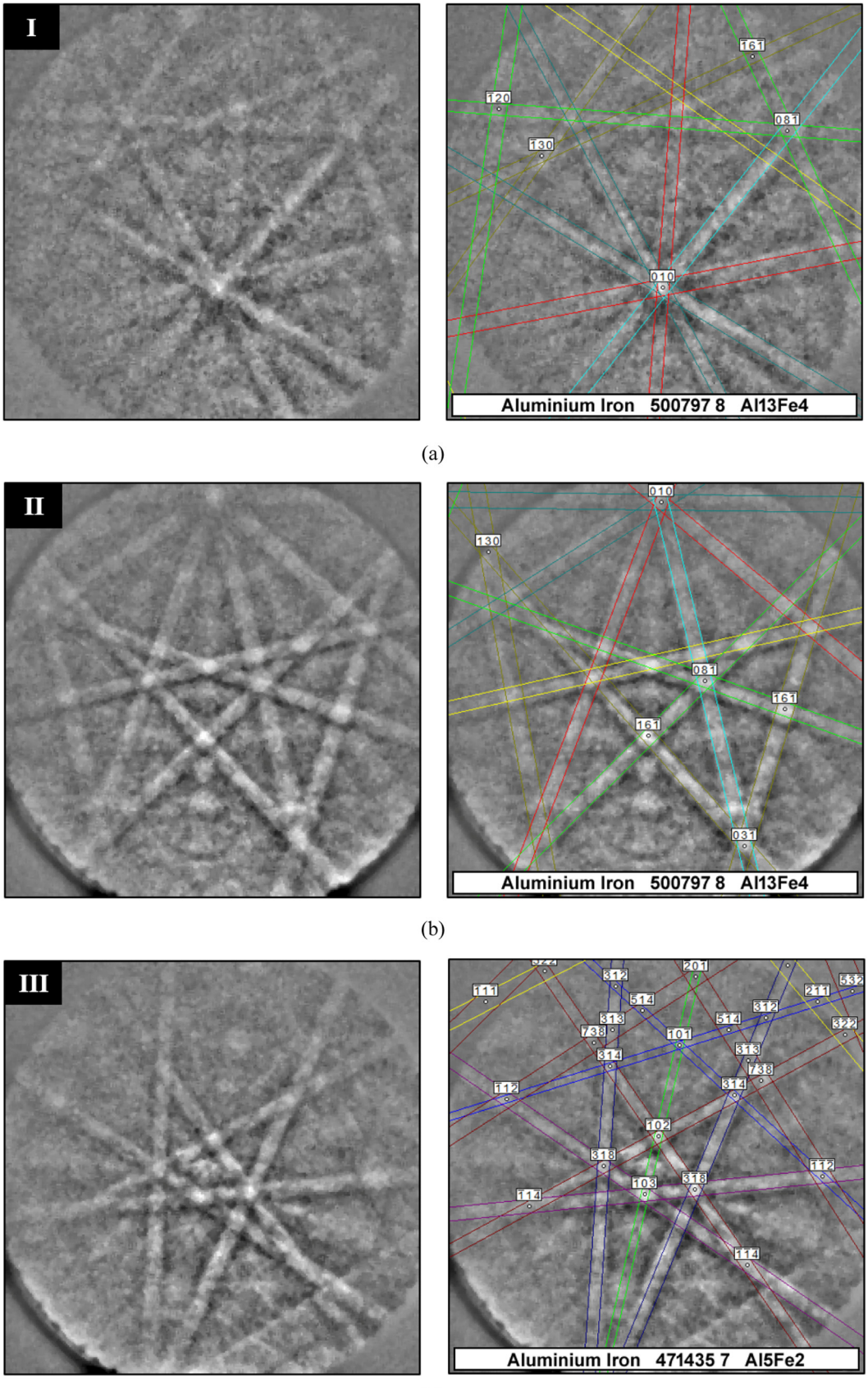

Fig. 5. EBSD diffraction patterns (and their indexed results) registered in the transition layer of the EE-HG6 weld: (a) Analysis zone I; (b) Analysis zone II; (c) Analysis zone III.

Table 5
Hardness values registered in the transition regions of the EE-PS5, EE-HG6 and AF-9 welds.

Hardness peaks ($HV_{0.025}$)		
EE-PS5	*EE-HG6*	*AF-9*
595	917	271
534	866	247
478	442	202
263	341	175

Table 6
Calculated ΔKE values for the EE and AF welds.

Weld	ΔKE ($10^6 J{\cdot}m^{-2}$)
EE-PS5	1.6
EE-HG6	2.9
AF-9	1.9
AF-6	1.0

The formation of a continuous interfacial layer prevented the effective joining of the metals in the EE welds. This shows that explosive mixtures with lower detonation velocities, such as ANFO, are more suitable for producing Fe-Al welds with a consistent structure. However, a sufficiently high explosive ratio should be used to promote consistent bonding along all the weld length. It is also important to stress that, although the energy lost in collision is an important parameter to analyse the welding conditions experienced at the weld interface, it is necessary to analyse it together with the detonation/collision point velocity.

3.5. Analysis of the Intermetallic Phases and Weldability

Besides the Wittman condition [18], which was used to define the top limit of the weldability window in Fig. 1, other theories addressing the upper boundary of the weldable region exist in the literature. According to Zakharenko [34] and Efremov and Zakharenko [35], the production of consistent joints, with effective interfacial bonding, requires that the molten material at the weld interface solidifies before tensile-stress waves arrive at this zone, i.e. the solidification time of the molten metal must be lower than the time needed for existing positive pressures at the weld interface. Otherwise, the positive pressures are sufficient to fracture the interfacial bonding already achieved. The expressions proposed by these authors for computing the time needed for existing positive pressures at the weld interface (t_p) and the solidification time of the molten metal (t_s) are displayed in Eqs. (07) and (08), respectively.

$$t_p = \left[0.5 + 0.66\left(\frac{\rho_{flyer}\cdot V_c^{\,2}}{G_{flyer}}\right)\right]\cdot\frac{\delta_{flyer}}{V_c} \tag{07}$$

G_{flyer} is the shear modulus (Pa) of the flyer plate.

$$t_s = \frac{Q^2}{4\cdot\pi\cdot c_{flyer}\cdot\lambda_{flyer}\cdot\rho_{flyer}\cdot T_{mflyer}^{\,2}},$$

$$Q = 6.8\cdot10^{-2}\cdot V_c^2\cdot\rho_{flyer}\cdot\delta_{flyer}\cdot\frac{\delta_{base}}{\delta_{flyer}+\delta_{base}}\cdot\sin^2\left(\frac{\beta}{2}\right) \tag{08}$$

Q is the heat released at the weld interface ($J{\cdot}m^{-2}$). δ_{base} is the thickness of the baseplate (m).

Although these expressions were developed for similar welding, in which formation of intermetallic phases usually does not occur, they have already been used in dissimilar welding [36, 37]. Table 7 shows the t_p and t_s values calculated for the EE and AF welds. The table also shows the difference calculated between both parameters ($\Delta t = t_p - t_s$) and the critical collision point velocity ($V_c{}^*$) for each weld, i.e. the maximum velocity that enables the production of a consistent joint (calculated for the condition $t_p = t_s$). For the AF welds, it can be observed that t_p is longer than t_s, indicating consistent joining, which agrees well with the interfacial properties of these joints. On the other hand, the values calculated for the EE welds are not in agreement with their structural properties. Although the table shows that t_p was longer than t_s (and $V_c{}^*$ is higher than the measured V_c) for both welds, effective bonding was not achieved in any of these joints.

Table 7
t_s, t_p, Δt and $V_c{}^*$ values obtained for the EE and AF welds.

Weld	t_p (μs)	t_s (μs)	Δt (μs)	$V_c{}^*(m{\cdot}s^{-1})$
EE-PS5	1.09	0.31	0.78	4467
EE-HG6	1.11	0.98	0.13	3642
AF-9	1.10	0.43	0.67	2903
AF-6	1.13	0.12	1.01	3601

The results displayed in the table can be better observed in Fig. 6, which shows the time-velocity diagrams obtained for all welds, i.e. the graphical evolution of t_p (black curve) and t_s (green curve) with the collision point velocity. The intersection point of both curves corresponds to $V_c{}^*$ and the vertical line represents the collision point velocity effectively measured for these welds. When the collision point velocity of the weld intersects the green shaded area, which corresponds to the weldable region, consistent joining is expected by this criterion.

From Table 7 and Fig. 6, it can be concluded that this criterion was more reliable for analysing the AF welds than the EE welds. In fact, the time-velocity diagrams obtained for the EE welds (Fig. 6a and b) are not in agreement with the experimental results, as they indicate that consistent welds should have been obtained. In turn, the diagrams for the AF welds (Fig. 6c and d) agree with the experimental results. As this criterion was developed for similar welding, its effectiveness in the AF welds results from the reduced interaction occurring at the interface of these welds, in which significant formation of intermetallic phases was not registered. Eq. (08) shows that the solidification time of the interfacial molten metal depends on the physical properties of the flyer plate, specifically, the specific heat, the thermal conductivity, the density, and the melting temperature. This is not valid in welds where the interfacial molten layer is thick and essentially composed of intermetallic material, with different physical properties from the welded materials (like the EE welds). The solidification time corresponding to the EE welds should be computed considering the physical properties of the transition material. So, Eq. (08) should be replaced by Eq. (09). This equation was achieved by assuming that the heat released by the impact at the weld interface (Q) remains the same and by replacing the physical properties of the flyer plate with those of the transition material.

$$t_s{}' = \frac{Q^2}{4\cdot\pi\cdot c_{TM}\cdot\lambda_{TM}\cdot\rho_{TM}\cdot T_{mTM}^{\,2}} \tag{09}$$

c_{TM}, λ_{TM}, ρ_{TM}, T_{mTM} are the specific heat ($J{\cdot}kg^{-1}{\cdot}K^{-1}$), the thermal conductivity ($W{\cdot}m^{-1}{\cdot}K^{-1}$), the density ($kg{\cdot}m^{-3}$) and the melting temperature (°C) of the transition material.

The Fe-Al system contains five equilibrium intermetallic phases, whose physical properties are displayed in Table 8. The physical properties of the welded materials are also displayed in the table. The information regarding the physical properties of the intermetallic phases is very limited and some scattering of values exists in the literature. An accurate analysis of the solidification time of the molten volume cannot be made, as it is likely that it does not depend only on the physical properties of the transition material, but also on the properties of the neighbouring metals, i.e. the flyer and the baseplate. Furthermore, the transition regions are not fully homogeneous, and the physical properties of the mixture are difficult to know. However, a trend regarding the effect of the formation of a low melting temperature and low thermal conductivity transition material on the Fe-Al

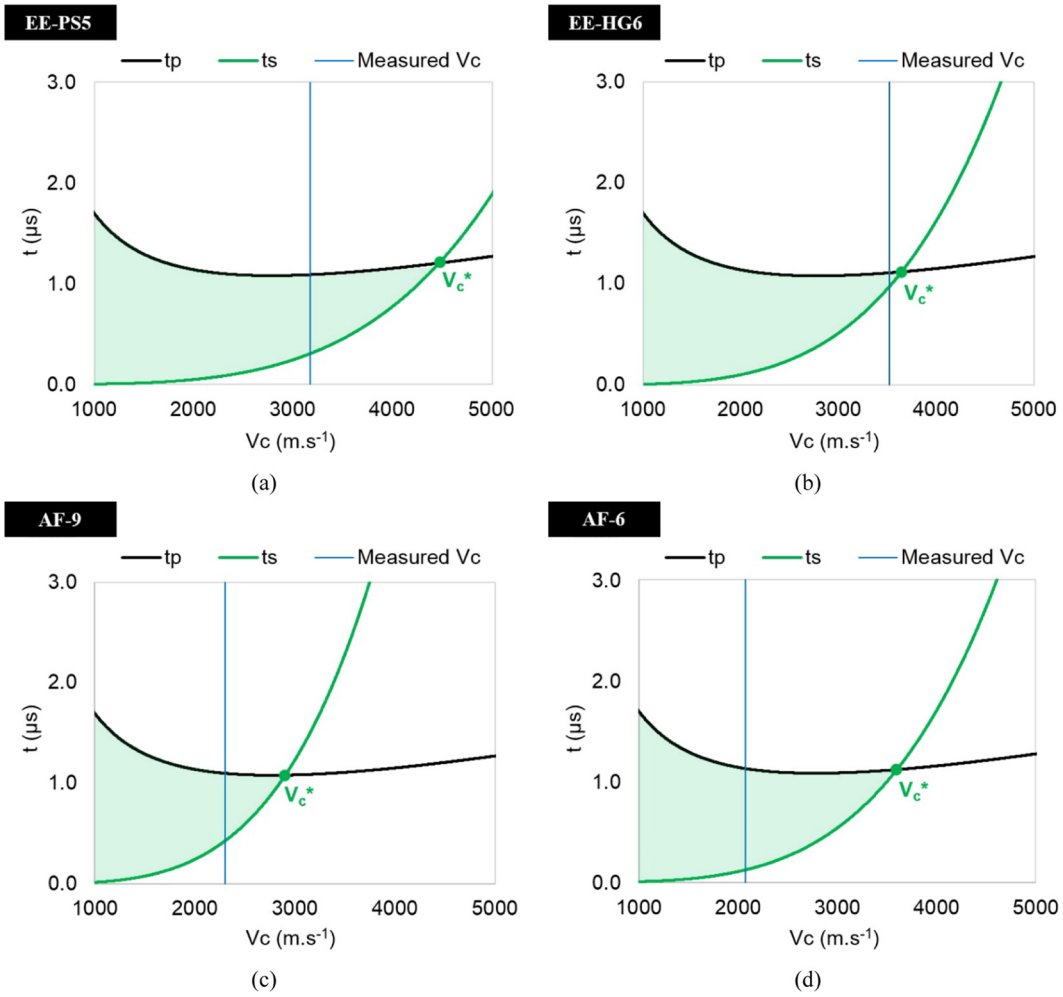

Fig. 6. Time-velocity diagrams obtained for the welds: (a) EE-PS5; (b) EE-HG6; (c) AF-9; (d) AF-6. (For interpretation of the references to color in this figure, the reader is referred to the web version of this article.)

Table 8
Physical properties of the Fe-Al equilibrium phases and the welded alloys.

Phases	Melting temp. (°C)	Density ($kg{\cdot}m^{-3}$)	Specific heat ($J{\cdot}kg^{-1}{\cdot}K^{-1}$)	Thermal conduct. ($W{\cdot}m^{-1}{\cdot}K^{-1}$)
Fe_3Al	1490 [38]	6660 [38]	560 [41]	14 [42]
	1502 [39]	6580 [40]		10.5 [40]
	1510 [40]			
FeAl	1250 [38]	5650 [38]	600 [43]	12 [43]
	1215 [39]	6000 [43]	560 [45]	12 [46]
		5580 [44]	640 [41]	10 [45]
$FeAl_2$	1164 [39]	4150 [44]	637.5 [47]	7 [49]
			631 [48]	
Fe_2Al_5	1171 [39]	7900 [44]	637.5 [47]	4 [51]
	1158 [50]			
Fe_4Al_{13}	1147 [52]	3896 [52]	675 [47]	3 [51]
	1152 [53]	3850 [44]	679 [48]	
	1150 [50]			
DC06 steel	1497 [54]	7856 [54]	470 [54]	67 [54]
AA6082	650 [55]	2700 [55]	897 [55]	180 [55]

weldability can be observed.

The new t_s' curves corresponding to the EE welds were plotted in the graphs illustrated in Fig. 7a (EE-PS5) and 7b (EE-HG6) (t_s' - red dashed curves; original t_s - green solid curve). Each curve was computed considering a homogeneous transition volume composed of one of the five Al-Fe equilibrium phases. As shown in the figure, a significant increase in the solidification time was registered for both welds, which promoted a considerable decrease in the critical collision point velocity (V_c*'). Much more restrictive conditions are obtained when aluminium-rich intermetallic volumes are generated at the weld interface, which was observed in the EE welds (Fe_4Al_{13}-rich transition layer). This analysis demonstrates that, in the dissimilar welding of metals with a high affinity to form intermetallic phases, the welding conditions are not only influenced by the properties of the welded metals and their relative

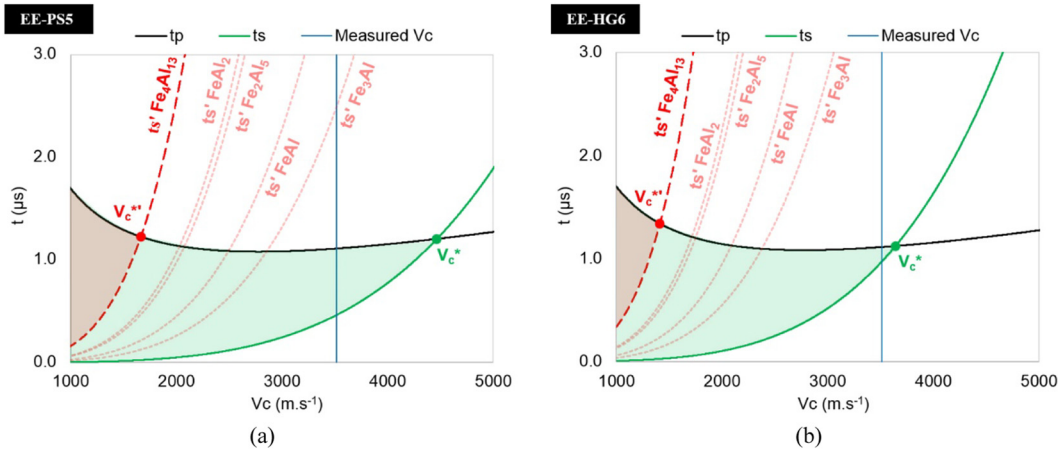

Fig. 7. Revised time-velocity diagrams obtained for the welds: (a) EE-PS5; (b) EE-HG6. (For interpretation of the references to color in this figure legend, the reader is referred to the web version of this article.)

positioning in the joint. The physical properties of the new phases generated at the weld interface significantly affect the achievement of sound welds. The detrimental effect of these phases on the Fe-Al weldability goes well beyond their brittle nature.

4. Conclusions

The formation of intermetallic structures at the interface of steel-to-aluminium explosive welds and their influence on the weldability of these two materials were studied in the present work. The following conclusions were drawn:

- Explosive mixtures with a lower detonation velocity are more suitable for producing steel-to-aluminium welds with a consistent bonding. Jet entrapment is prevented under these conditions, and continuous molten layers are not formed at the weld interface.
- In welding steel-to-aluminium, the welding requirements are not only influenced by the properties of the metals to be welded. The physical properties of the new phases generated at the weld interface have a significant influence on the weldability of these materials.
- The formation of aluminium-rich intermetallic phases at the interface of steel-to-aluminium explosive welds increases the solidification time of the transition molten material, decreasing the weldability of these two metals. Therefore, intermetallic compounds should be avoided by reducing the interaction between the flyer and the baseplate materials, as well as by avoiding large molten layers in the process.

Acknowledgements

This research is sponsored by FEDER funds through the programme COMPETE - *Programa Operacional Factores de Competitividade* - and by national funds through FCT - *Fundação Portuguesa para a Ciência e a Tecnologia*, under the project UID/EMS/00285/2013. The authors also acknowledge the financial support of the IPL - *Instituto Politécnico de Lisboa*, under the project IPL/2017/EWDMat/ISEL. The first author, G.H.S.F.L. Carvalho, is supported by CNPq - *Conselho Nacional Brasileiro de Desenvolvimento Científico e Tecnológico*.

Data Availability

The raw and processed data required to reproduce these findings cannot be shared at this time due to technical/time limitations.

References

[1] F. Findik, Recent developments in explosive welding, Mater. Des. 32 (3) (2011) 1081–1093.
[2] A. Kapil, A. Sharma, Magnetic pulse welding: an efficient and environmentally friendly multi-material joining technique, J. Clean. Prod. 100 (2015) 35–58.
[3] I.A. Bataev, D.V. Lazurenko, S. Tanaka, K. Hokamoto, A.A. Bataev, Y. Guo, A.M.J. Jr, High cooling rates and metastable phases at the interfaces of explosively welded materials, Acta Mater. 135 (2017) 277–289.
[4] L. Tricarico, R. Spina, D. Sorgente, M. Brandizzi, Effects of heat treatments on mechanical properties of Fe/Al explosion-welded structural transition joints, Mater. Des. 30 (7) (2009) 2693–2700.
[5] H. Yu, Z. Fan, C. Li, Magnetic pulse cladding of aluminum alloy on mild steel tube, J. Mater. Process. Technol. 214 (2) (2014) 141–150.
[6] H. Yu, Y. Tong, Magnetic pulse welding of aluminum to steel using uniform pressure electromagnetic actuator, Int. J. Adv. Manuf. Technol. 91 (5–8) (2017) 2257–2265.
[7] X. Li, H. Ma, Z. Shen, Research on explosive welding of aluminum alloy to steel with dovetail grooves, Mater. Des. 87 (2015) 815–824.
[8] Y. Aizawa, J. Nishiwaki, Y. Harada, S. Muraishi, S. Kumai, Experimental and numerical analysis of the formation behavior of intermediate layers at explosive welded Al/Fe joint interfaces, J. Manuf. Process. 24 (1) (2016) 100–106.
[9] Z. Fan, H. Yu, C. Li, Interface and grain-boundary amorphization in the Al/Fe bimetallic system during pulsed-magnetic-driven impact, Scr. Mater. 110 (2016) 14–18.
[10] H. Yu, H. Dang, Y. Qiu, Interfacial microstructure of stainless steel/aluminum alloy tube lap joints fabricated via magnetic pulse welding, J. Mater. Process. Technol. 250 (2017) 297–303.
[11] R. Mendes, J. Ribeiro, I. Plaksin, J. Campos, B. Tavares, Differences between the detonation behavior of emulsion explosives sensitized with glass or with polymeric micro-balloons, J. Phys. Conf. Ser. 500 (2014) 2–8.
[12] R. Mendes, J.B. Ribeiro, A. Loureiro, Effect of explosive characteristics on the explosive welding of stainless steel to carbon steel in cylindrical configuration, Mater. Des. 51 (2013) 182–192.
[13] H. El-Sobky, Mechanics of explosive welding, in: T.Z. Blazynski (Ed.), Explosive Welding, Forming and Compaction, Applied Science Publishers, Essex, 1983, pp. 189–217.
[14] J.E. Kennedy, Gurney Energy of Explosives: Estimation of the Velocity and Impulse Imparted to Driven Metal, Sandia National Laboratories, New Mexico, 1970.
[15] P.W. Cooper, Explosives Engineering, Wiley-VCH, USA, 1996.
[16] G.R. Cowan, O.R. Bergmann, A.H. Holtzman, Mechanism of bond zone wave formation in explosion-clad metals, Metall. Trans. A. 2 (11) (1971) 3145–3155.
[17] A.A. Deribas, I.D. Zakharenko, Surface effects with oblique collisions between metallic plates, Combust. Explos. Shock Waves 10 (3) (1974) 358–367.
[18] S.H. Carpenter, R.H. Wittman, Explosion welding, Annu. Rev. Mater. Sci. 5 (1975) 177–199.
[19] J.M. Walsh, R.G. Shreffler, F.J. Willig, Limiting conditions for jet formation in high velocity collisions, J. Appl. Phys. 24 (3) (1953) 349–359.
[20] W.S.D. Rosset, Analysis of explosive bonding parameters, Mater. Manuf. Process. 21 (6) (2006) 634–638.
[21] G.H.S.F.L. Carvalho, I. Galvão, R. Mendes, R.M. Leal, A. Loureiro, Influence of base material properties on copper and aluminium–copper explosive welds, Sci. Technol. Weld. Join. 23 (2018) 501–507.
[22] A. Szecket, O.T. Inal, D.J. Vigueras, J. Rocco, A wavy versus straight interface in the explosive welding of aluminum to steel, J. Vac. Sci. Technol. A 3 (6) (1985) 2588–2593.
[23] A. Loureiro, R. Mendes, J.B. Ribeiro, R.M. Leal, I. Galvão, Effect of explosive mixture on quality of explosive welds of copper to aluminium, Mater. Des. 95 (2016) 256–267.
[24] G.H.S.F.L. Carvalho, R. Mendes, R.M. Leal, I. Galvão, A. Loureiro, Effect of the flyer

material on the interface phenomena in aluminium and copper explosive welds, Mater. Des. 122 (2017) 172–183.
[25] H. Paul, L. Litynska-Dobrzynska, M. Prazmowski, Microstructure and phase constitution near the interface of explosively welded aluminum/copper plates, Metall. Mater. Trans. A 44 (8) (2013) 3836–3851.
[26] G. Sauthoff, Deformation of intermetallic alloys at high temperatures, in: E. Belin-Ferré (Ed.), Mechanical Properties of Complex Intermetallics, World Scientific Publishing, Singapore, 2011.
[27] P. Matysik, S. Jóźwiak, T. Czujko, Characterization of low-symmetry structures from phase equilibrium of fe-al system — microstructures and mechanical properties, Materials 8 (3) (2015) 914–931.
[28] M.J. Rathod, M. Kutsuna, Joining of aluminum alloy 5052 and low-carbon steel by laser roll welding, Weld. J. 83 (2004) 16s–26s.
[29] K. Hokamoto, T. Izuma, M. Fujita, New explosive welding technique to weld aluminum alloy and stainless steel plates using a stainless steel intermediate plate, Metall. Mater. Trans. A 24 (10) (1993) 2289–2297.
[30] K. Hokamoto, A. Chiba, M. Nishida, M. Fujita, Experimental conditions for fabrication of multilayered metal base composites by single-shot explosive welding, Weld. Int. 9 (2) (1995) 116–120.
[31] I. Plaksin, J. Campos, J. Ribeiro, R. Mendes, J. Direito, D. Braga, R. Pruemmer, Novelties in physics of explosives welding and powder compaction, J. Phys. IV 110 (2003) 797–802.
[32] M.D. Chadwick, P.W. Jackson, Explosive welding in planar geometries, in: T.Z. Blazynski (Ed.), Explosive Welding, Forming and Compaction, Applied Science Publishers, Essex, 1983, pp. 189–217.
[33] G.R. Cowan, A.H. Holtzman, Flow configurations in colliding plates: explosive bonding, J. Appl. Phys. 34 (4) (1963) 928–939.
[34] I.D. Zakharenko, Critical conditions in detonation welding, Combust. Explos. Shock Waves 8 (3) (1972) 422–427.
[35] V.V. Efremov, I.D. Zakharenko, Determination of the upper limit to explosive welding, Combust. Explos. Shock Waves 12 (2) (1976) 255–260.
[36] S. Saravanan, K. Raghukandan, Thermal kinetics in explosive cladding of dissimilar metals, Sci. Technol. Weld. Join. 17 (2) (2012) 99–103.
[37] V.I. Kuz'min, V.I. Lysak, A.N. Kriventsov, M.A. Yakovlev, Critical conditions of the formation and failure of welded joints in explosive welding, Weld. Int. 18 (3) (2004) 223–227.
[38] M. Eggersmann, H. Mehrer, Diffusion in intermetallic phases of the Fe-Al system, Philos. Mag. A 80 (5) (2000) 1219–1244.
[39] S.C. Deevi, V.K. Sikka, Nickel and iron aluminides: an overview on properties, processing, and applications, Intermetallics 4 (5) (1996) 357–375.
[40] C.G. McKamey, Behavior of alloy systems - iron aluminides, in: N.S. Stoloff, V.K. Sikka (Eds.), Physical Metallurgy and Processing of Intermetallic Compounds, Chapman & Hall, New York, 1996, pp. 351–391.
[41] M. Kass, C.R. Brooks, D. Falcon, D. Basak, The formation of defects in Fe-Al alloys: electrical resistivity and specific heat measurements, Intermetallics 10 (10) (2002) 951–966.
[42] S. Hanai, Y. Terada, K. Ohkubo, T. Mohri, T. Suzuki, Thermal conductivity in A3B intermetallic compounds based on iron and nickel, Intermetallics 4 (Supplement 1) (1996) S41–S47.
[43] Y. Terada, K. Ohkubo, K. Nakagawa, T. Mohri, T. Suzuki, Thermal conductivity of B2-type aluminides and titanides, Intermetallics 3 (5) (1995) 347–355.
[44] P. Villars, Pauling File, Inorganic Solid Phases, SpringerMaterials (online database), Springer, Heidelberg, 2016.
[45] B.V. Reddy, S.C. Deevi, Thermophysical properties of FeAl (Fe-40 at.% Al), Intermetallics 8 (12) (2000) 1369–1376.
[46] Y. Terada, K. Ohkubo, T. Mohri, T. Suzuki, Thermal conductivity of intermetallic compounds with metallic bonding, Mater. Trans. 43 (12) (2002) 3167–3176.
[47] M. Rank, P. Gotcu, P. Franke, H.J. Seifert, Thermodynamic investigations in the Al-Fe system: heat capacity measurements of three intermetallic phases, Intermetallics 94 (2018) 73–82.
[48] T. Zienert, A. Leineweber, O. Fabrichnaya, Heat capacity of Fe-Al intermetallics: B2-FeAl, FeAl2, Fe2Al5 and Fe4Al13, J. Alloys Compd. 725 (2017) 848–859.
[49] C.S. Lue, Y.K. Kuo, Thermal and electrical transport properties of ordered FeAl2, J. Phys. Condens. Matter 15 (6) (2003) 877–882.
[50] X. Li, A. Scherf, M. Heilmaier, F. Stein, The Al-rich part of the Fe-Al phase diagram, J. Phase Equilib. Diffus. 37 (2) (2016) 162–173.
[51] K. Tobita, N. Sato, K. Kitahara, Y. Takagiwa, K. Kimura, Effect of anomalous crystal structure of iron aluminides Fe2Al5 and Fe4Al13: low phonon thermal conductivity and potentiality as thermoelectric materials, Mater. Trans. 57 (7) (2016) 1045–1049.
[52] L.F. Mondolfo, Aluminum Alloys: Structure and Properties, Butterworth, Beccles and London, 1976.
[53] MSIT, G. Ghosh, Aluminium - iron - silicon, in: G. Effenberg, S. Ilyenko (Eds.), Ternary Alloy Systems: Phase Diagrams, Crystallographic and Thermodynamic Data - Iron Systems, Part 1, Springer, Heidelberg, 2008, pp. 184–266.
[54] M. Spittel, T. Spittel, Steel symbol/number:DC06/1.0873, in: H. Warlimont (Ed.), Metal Forming Data of Ferrous Alloys - Deformation Behaviour, Springer, Heidelberg, 2009.
[55] ASM (Ed.), Properties and Selection: Nonferrous Alloys and Special-purpose Materials, 10th ed., ASM International, Materials Park - Ohio, 1990.